

# Adsorption Coupling Photocatalytic Removal of Gaseous n-Hexane by Phosphorus Doped g-C<sub>3</sub>N<sub>4</sub>/TiO<sub>2</sub>/Zn(OAc)<sub>2</sub>-ACF Composites

EnCheng Sun

technology inspection center of shengli oil field

Haidi Wei (✉ [1656887023@qq.com](mailto:1656887023@qq.com))

China University of Petroleum Huadong - Qingdao Campus <https://orcid.org/0000-0003-4006-284X>

Shuai Zhang

China University of Petroleum Huadong - Qingdao Campus

Yuxi Bi

China University of Petroleum Huadong - Qingdao Campus

Ziyan Huang

Hubei University

Guoyang Ji

China University of Petroleum Huadong - Qingdao Campus

Fang Liu

China University of Petroleum Huadong - Qingdao Campus <https://orcid.org/0000-0001-6509-3701>

Chaocheng Zhao

China University of Petroleum Huadong - Qingdao Campus

---

## Research Article

**Keywords:** N-hexane, Adsorption coupled photocatalytic degradation, Phosphorus doping, Carbon nitride, Zinc acetate modified activated carbon fiber, S-scheme heterojunction

**Posted Date:** May 10th, 2022

**DOI:** <https://doi.org/10.21203/rs.3.rs-1529416/v1>

**License:** © ⓘ This work is licensed under a Creative Commons Attribution 4.0 International License.

[Read Full License](#)

---

# Abstract

VOCs emission reduction in the petroleum and petrochemical industry is a hot and difficult topic at present. The single method may not be able to meet the actual treatment status. Therefore, the adsorption coupled photocatalytic degradation technology was used to remove VOCs. Phosphorus doped carbon nitride (PCN) and PCN/TiO<sub>2</sub> were prepared by hydrothermal synthesis and sol-gel method, and then PCN/TiO<sub>2</sub>/Zn(OAc)<sub>2</sub>-ACF composites were prepared by ultrasonic impregnation on zinc acetate modified activated carbon fibers (Zn(OAc)<sub>2</sub>-ACF). The removal efficiency of n-Hexane by composite materials was explored in a self-made reactor, and the factors affecting, removal efficiency, removal mechanism and possible ways of degradation were investigated. The results showed that under the optimum reaction conditions (initial concentration of n-hexane 200 mg/m<sup>3</sup>, space velocity 1000 h<sup>-1</sup>, light intensity 24 W, mass fraction of doped PCN 6%, loading twice, calcination temperature 450 °C), PCN/TiO<sub>2</sub>/Zn(OAc)<sub>2</sub>-ACF composite has the highest removal efficiency of n-hexane (90.2%). The adsorption capacity of the composites after doping the P element was 215.3 mg/g, which didn't enhance the adsorption performance compared with that before doping, but the removal rate of n-hexane was higher. This showed that doping P element was helpful to enhance the photocatalytic activity of the composites.

## 1. Introduction

Volatile organic compounds (VOCs) are common gaseous environmental pollutants, mainly in the petroleum and petrochemical industry, printing, automobile exhaust, coating manufacturing, and other industries. They can be divided into alkanes, aromatics, olefins, halogenated hydrocarbons, esters, aldehydes and ketones (Sekar, Varghese, & Ravi Varma, 2019; Xinmin Zhang et al., 2017). Alkanes are the main composition of VOCs emitted artificially, accounting for about 40% of the anthropogenic emissions (Wei et al., 2019; Ziemann, 2011). N-hexane (C<sub>6</sub>H<sub>14</sub>) is a widely used alkane in industry and the most representative nonpolar solvent. It usually exists in oil in the form of saturated fatty hydrocarbons and can be separated from natural gas and oil fractionation. N-hexane is highly fat-soluble and easy to accumulate in organisms. Long-term exposure can lead to chronic poisoning symptoms such as headache, dizziness and numbness of limbs (Y. Guo et al., 2022; Yang et al., 2019). In serious cases, it can lead to loss of consciousness, cancer and even death. In addition, it can promote the generation of secondary organic aerosols, resulting in photochemical smog, seriously affecting air quality and human health, so it is urgent to deal with it (Thanh Truc et al., 2019; Yu et al., 2020).

Several VOCs control techniques including photocatalytic oxidation (PCO), adsorption, membrane filtration and catalytic combustion have been developed and used to treat alkane (Zhao et al., 2019; Ziemann, 2011). Generally, the membrane separation efficiency is not high. The energy consumption of catalytic combustion is very high. Therefore, there is a great challenge to design novel catalysts with the dual effects of photodegradation and adsorption for removal (Tian, Liao, Ke, Guo, & Guo, 2017).

Adsorption technology is the most effective and has been widely used. Activated carbon, activated alumina, silica gel and zeolite are commonly used adsorbents (T. Guo, Bai, Wu, & Zhu, 2008; Shi, Zheng, Wu, & Ji, 2008). Activated carbon fiber (ACF) is an effective VOCs adsorbent. ACF has many advantages, such as high surface adsorption reactivity, uniform microporous structure, renewability, large specific surface area and no secondary pollution (Das, Gaur, & Verma, 2004; Lin, Cheng, Liu, & Chen, 2012; Z. S. Liu, Peng, & Li, 2014; Miyamoto, Kaneko, & Kanoh, 2005; Yi, Lin, Chen, & Wei, 2008). To improve the adsorption effect and selectivity, it is often necessary to adjust the pore structure of ACF or modify its surface characteristics. At present, the commonly used modification methods are surface oxidation-reduction, supported metal and metal oxide (Yi et al., 2008). Bi et al. (Bi et al., 2021) modified activated carbon fiber (ACF) with  $\text{Zn}(\text{NO}_3)_2$ ,  $\text{ZnCl}_2$  and  $\text{Zn}(\text{OAc})_2$ , respectively, and then loaded  $\text{TiO}_2$  on the modified ACF. The experiment showed that  $\text{TiO}_2/\text{Zn}(\text{OAc})_2\text{-ACF}$  had the best toluene degradation performance.

Photocatalytic technology has the advantages of high efficiency, energy-saving, safety, low cost and mild reaction conditions, which is widely used to treat sewage and gas pollution (C. Hou, Liu, & Li, 2021; Mamaghani, Haghghat, & Lee, 2017). However, photocatalytic oxidation technology has the disadvantages of catalyst deactivation, easy recombination of photogenerated electrons and holes, and easy agglomeration of carriers. The commonly used catalysts include  $\text{TiO}_2$ ,  $\text{g-C}_3\text{N}_4$ , bismuth-based materials, graphene and its composites (Fu, Xu, Low, Jiang, & Yu, 2019; Wang et al., 2019; Xie et al., 2019). Among many catalysts,  $\text{TiO}_2$  has attracted much attention in recent years due to its outstanding advantages such as low energy consumption, simple operation, wide application range and no secondary pollution. However, due to the wide bandgap (3.2 eV), pure  $\text{TiO}_2$  can only absorb ultraviolet light with a short wavelength, and the utilization of solar energy is poor (Raja, Rajasekaran, Selvakumar, Ganapathi Raman, & Swaminathan, 2020). Therefore,  $\text{TiO}_2$  needs to be modified to improve its visible light response. There are many modification methods for  $\text{TiO}_2$ , such as noble metal modification, semiconductor composite, dye sensitization and transition metal ion doping (Q. H. Li et al., 2021). Graphitic carbon nitride ( $\text{g-C}_3\text{N}_4$ ) is a non-metallic semiconductor catalyst with excellent performance. The raw materials are cheap and easy to get (amino nitrile, urea, melamine, dicyandiamide), narrow bandgap (2.7 eV), good thermal and chemical stability (Wen et al., 2015) (Huang et al., 2019). In recent years,  $\text{g-C}_3\text{N}_4$  has become a research hotspot of the photocatalyst. However, the photocatalytic activity of  $\text{g-C}_3\text{N}_4$  was low because of its small specific surface area and the easy recombination of photogenerated electrons and holes (Fang et al., 2018; Humayun, Fu, Zheng, Li, & Luo, 2018). Accordingly, various methods have been reported to improve its photocatalytic performance, such as doping metal/non-metal elements, constructing heterostructures or optimizing morphology (Gao et al., 2019). Recently, some studies have shown that P doping in  $\text{g-C}_3\text{N}_4$  can significantly improve the photocatalytic performance of (Gao et al., 2019; Humayun et al., 2018; Z. Li, Jiang, Zhang, Wu, & Han, 2016; S. Liu, Zhu, Yao, Chen, & Chen, 2018; Wu, Ma, & Hu, 2020). For example, the phosphorus (P) doped  $\text{g-C}_3\text{N}_4$  synthesized by a simple sintering method showed an obvious red shift at the absorption edge (Wu et al., 2020). Li et al. (Z. Li et al., 2016) prepared P (x%)- $\text{g-C}_3\text{N}_4/\text{TiO}_2$  composites showed enhanced light absorption and photocatalytic

properties in the visible light region, and had high photocatalytic degradation activity for methyl blue (MB).

Another difficult problem of VOCs photocatalytic oxidation degradation technology is that powder photocatalytic materials are difficult to apply and recover due to the fluidity of gas. To solve the above problems, the powder material needs to be loaded on ACF. Previous studies have shown that the strong adsorption performance of ACF can not only enrich target pollutants, capture intermediate toxic products, promote the photocatalytic performance of nano-TiO<sub>2</sub>, but also provide support for the renewable performance of TiO<sub>2</sub> photocatalytic materials. In addition, metal oxide-based catalysts loaded on ACF can provide a large number of binding sites on the surface of the adsorbent, which significantly improves the adsorption performance of ACF. Moreover, the introduction of catalyst reduces the blockage of ACF microporous structure, promotes the in-situ regeneration of adsorbent, and reduces the risk of adsorbent failure due to the increase of adsorption concentration (T. Guo et al., 2008; Shi et al., 2008; Tran Thi & Lee, 2017).

Under the guidance of the above strategies, TiO<sub>2</sub> modified by the P-doped g-C<sub>3</sub>N<sub>4</sub> photocatalyst was prepared by the sol-gel method in this work. PCN/TiO<sub>2</sub>/Zn(OAc)<sub>2</sub>-ACF composites were prepared by ultrasonic impregnation on zinc acetate modified ACF. Then, by exploring the effects of different factors (calcination temperature, impregnation times, light intensity, initial concentration of n-hexane, etc.) on PCN/TiO<sub>2</sub>/Zn(OAc)<sub>2</sub>-ACF's degradation of n-hexane, the adsorption and photocatalytic mechanism of the catalyst were further studied.

## 2. Experimental Section

### 2.1 Materials

Activated carbon fiber (ACF) was purchased from Nantong Senyou Carbon Fiber Co., Ltd. Concentrated nitric acid (HNO<sub>3</sub>, 68%), zinc acetate (Zn(OAc)<sub>2</sub>, AR), zinc chloride (ZnCl<sub>2</sub>, AR), anhydrous ethanol (C<sub>2</sub>H<sub>6</sub>O, AR), acetic acid (CH<sub>3</sub>COOH), tetrabutyl titanate (C<sub>6</sub>H<sub>36</sub>O<sub>4</sub>Ti, TBOT, AR), sodium phosphate (Na<sub>3</sub>PO<sub>4</sub>) and carbon disulfide (CS<sub>2</sub>, AR) were supplied by Sinopharm Chemical Reagent Co., Ltd.

### 2.2 Preparation of ACF modified by zinc acetate (Zn(OAc)<sub>2</sub>-ACF)

Firstly, ACF was pretreated. The ACF with the shape of 2 cm \* 2 cm was soaked and washed three times in an 8% ethanol solution to remove organic matter and impurities. Then the product was boiled in deionized water for 2 h. In this process, deionized water was changed every half hour. The pretreated ACF was taken out and dried in an oven at 105°C to obtain the pretreated ACF. Then the pretreated ACF was put into a 100ml beaker containing 50ml Zn(OAc)<sub>2</sub> (0.01mol/L) solution. Then, in order to make the solution uniformly and fully soak ACF, the beaker was placed in the vacuum chamber for 10 min, and the

ultrasonic-vacuum impregnation process was repeated twice. Finally, the impregnated ACF was dried at 105°C and marked as Zn(OAc)<sub>2</sub>-ACF.

## 2.3 Preparation of PCN material

Phosphorus doped carbon nitride (PCN) was prepared by hydrothermal synthesis (Fig. 1 (a)). Melamine (C<sub>3</sub>H<sub>6</sub>N<sub>6</sub>) (1.26 g) was added to dimethyl sulfoxide (DMSO) (60 ml), and magnetically stirred to a uniform mixing and denoted as solution A, melamine (C<sub>3</sub>H<sub>3</sub>N<sub>3</sub>O<sub>3</sub>) (1.29 g) was added to DMSO (50 ml), and magnetically stirred to a uniform mixing and denoted as solution B. Drop solution B slowly into solution A with uniform stirring speed. The mixed solution was centrifuged in a high-speed centrifuge and washed three times with anhydrous ethanol and water, respectively. The centrifugal product was put into the hydrothermal synthesis reactor, adding 60 ml water and 0.01 mol (3.92 g) sodium phosphate, stirring for 2 h, and then heating at 180°C for 8 h. The precursor was obtained by centrifugal drying of the material. The precursor was heated at 450°C for 4 h in a tube furnace protected by nitrogen to obtain phosphorus-doped carbon nitride (PCN).

## 2.4 Preparation of PCN/TiO<sub>2</sub>/Zn(OAc)<sub>2</sub>-ACF Composites

PCN/TiO<sub>2</sub>/Zn(OAc)<sub>2</sub>-ACF Composites were prepared by sol-gel method (Fig. 1 (b)). Tetrabutyl titanate (10 mL), acetic acid (17 mL) and anhydrous ethanol (34 mL) were poured into a 250 mL beaker and stirred for 30 min, denoted as solution A. The PCN (TiO<sub>2</sub>: PCN mass ratio = 2%, 4%, 6%, 8%), anhydrous ethanol (10 mL), deionized water (30 mL) and acetic acid (2 mL) were poured into a 250 mL beaker and stirred for 30 min to obtain solution B. Slowly drop solution B into uniform stirring solution A, continue stirring for 2 h, standing for 24 h. The ACF modified by zinc acetate was put into the aging sol, ultrasonic for 5 minutes, impregnated for 30 minutes. Repeat the above steps. Then, the impregnated composite was calcined in a 450 ° C tubular furnace in a nitrogen atmosphere for 2 hours to obtain 2% PCN/TiO<sub>2</sub>/Zn(OAc)<sub>2</sub>-ACF, 4% PCN/TiO<sub>2</sub>/Zn(OAc)<sub>2</sub>-ACF, 6% PCN/TiO<sub>2</sub>/Zn(OAc)<sub>2</sub>-ACF and 8% PCN/TiO<sub>2</sub>/Zn(OAc)<sub>2</sub>-ACF respectively.

## 2.5 Characterization

The elemental composition and valence state of the surface of the composites were analyzed by an X-ray photoelectron spectrometer (XPS, Thermo Scientific, K-Alpha). The crystal structure and grain size of the composites were determined by X-ray diffraction spectra (XRD, PANalytical B.V., AXIOS-Petro) with power 2200 W, Cu-Kα radiation (λ = 1.54187 Å), scanning angle 10°~80°, step 0.02 °/s. The functional groups of the samples were characterized by Fourier transform infrared spectrometer (FTIR, Nicolet, Nexus). The size and morphology of the samples were observed by scanning electron microscope (SEM, Hitachi, S4800) with a scanning voltage of 50 kV. TEM was performed by using a JEM-2100UHR transmission electron microscope with analysis voltage of 200kV. Adsorption was carried out at 77.4 K with N<sub>2</sub> as adsorbate, and desorption occurred at 300 K. The specific surface area, pore size and pore volume distribution of the samples were measured by the analysis of Brunauer-Emmett-Teller (BET, ASAP3020, Mike Instruments Co.). The photoluminescence spectra of samples were measured by F97Pro

fluorescence spectrophotometer (Semerfeld, China). I-T photocurrent analysis can be used to determine the light response of materials. Samples/conductive glass is used as working electrode, platinum wire as a counter electrode, saturated calomel electrode as a reference electrode. The samples were subjected to visible light irradiation (300 W Xe lamp, Institute of Perfect Light sources, Beijing) and a photocurrent test at a bias voltage of 0.0 V. The optical absorption properties of the composites were measured by ultraviolet-visible diffuse reflectance spectrophotometer (UV-vis DRS, TU-1901, Beijing General Instrument Co.).

## 2.6 n-hexane removal experiment

The composites were fixed in the quartz tube reactor. Then, the self-assembly experimental device was operated under normal temperature and pressure, RH (relative humidity) = 50%, stable airflow and no pollutants. Then a dark reaction was carried out to make the composite completely absorb n-hexane (the initial concentration of 200 mg/m<sup>3</sup>). After reaching the adsorption equilibrium, the low-pressure mercury lamp was turned on for photocatalytic reaction. During the experiment, the inlet and outlet gas of n-hexane were sampled regularly by activated carbon sampling tube. And the effects of mass fraction of PCN, calcination temperature of composites, loading times, light source, light intensity, initial concentration of n-hexane and space velocity of n-hexane on the removal performance of composites were investigated.

The samples were resolved with carbon disulfide and injected into the gas chromatography (GC, SP-3420A) to determine the concentration of n-hexane. The removal efficiency of n-hexane (R) was calculated by Eq. (1):

$$R = (C_0 - C) / C_0 \times 100\%$$

1

where  $C_0$  (mg/m<sup>3</sup>) and  $C$  (mg/m<sup>3</sup>) respectively represent the concentration of n-hexane at the initial time and time  $t$ .

## 3. Results And Discussion

### 3.1. Characterization analysis

To further explore the chemical composition of the sample, the PCN is analyzed by XPS. XPS spectra (Fig. 2(a)) shows that PCN consists of four elements: C, N, O and P. The peaks at 284.51 and 287.86 in high-resolution C 1s XPS spectra (Fig. 2(b)) correspond to C-C and N-C = N. The high-resolution N 1s XPS spectrum (Fig. 2(c)) consists of three peaks, which can be assigned to C-N = C (398.29 eV), N- (C) 3 (399.92 eV) and N-H (400.94 eV). The peak at 531.80 in high-resolution O1s XPS spectra (Fig. 2(d)) corresponds to O-H. The peak at 132.20 in high-resolution P2p XPS spectra (Fig. 2(e)) corresponds to P-N(Z. Li et al., 2016). It is proved that P was successfully doped into the lattice of g-C<sub>3</sub>N<sub>4</sub>.

XRD and FTIR spectra are conducted to collect the crystalline and framework structure of the pristine and composite samples, the results are shown in Fig. 3(a) and (b). According to the PDF card (PDF#21-1272), the anatase phase characteristic diffraction peaks of  $\text{TiO}_2$  composites supported on modified ACFs with different zinc salts are observed at  $2\theta = 25.37^\circ, 38.60^\circ, 48.07^\circ, 54.10^\circ, 54.86^\circ, 62.58^\circ$ , corresponding to 101, 004, 200, 105, 211 and 204 crystal planes, respectively. The  $\text{g-C}_3\text{N}_4$  sample presents typical peaks at  $13.10^\circ$  and  $27.50^\circ$ , which are assigned to (1 0 0) and (0 0 2) planes (JCPDS 87e1526). The weak peak at  $13.10^\circ$  results from the in-planar structure of  $\text{g-C}_3\text{N}_4$ , while the peak at  $27.50^\circ$  could be ascribed to the stacking aromatic structure (Chen et al., 2020; J. Hou et al., 2012). The characteristic peak of the PCN sample is consistent with that of carbon nitride and has high peak strength, indicating that the crystallinity is increased. With the PCN ratio increasing,  $\text{TiO}_2$  diffraction peaks at  $25.4^\circ$  and  $27.5^\circ$  are shifting towards the low angle indicating the chemical interaction between PCN and  $\text{TiO}_2$ , which further confirms the PCN/ $\text{TiO}_2$  heterojunction formation. FT-IR spectra of PCN/ $\text{TiO}_2$ / $\text{Zn}(\text{OAc})_2$ -ACF composites are shown in Fig. 3(b). The spectra shows that all the spectra of the samples are the combination of characteristic peaks of  $\text{TiO}_2$  and  $\text{g-C}_3\text{N}_4$ . Specifically, the peak at about  $470\text{ cm}^{-1}$  is the characteristic peak of anatase  $\text{TiO}_2$ , which is attributed to the tensile vibration of Ti-O-Ti. The sharp absorption peak at  $806\text{ cm}^{-1}$  is attributed to the out-of-plane bending vibration of tri-s-triazine units of  $\text{g-C}_3\text{N}_4$ , and the strong absorption bands between  $1240$  and  $1640\text{ cm}^{-1}$  are attributed to the typical C-N and C = N stretching vibrations of the tris-s-triazine ring. The absorption bands between  $3000$  and  $3600\text{ cm}^{-1}$  are attributed to the O-H stretching vibration (Du, Bai, Xu, Yang, & Jin, 2020). As shown in Fig. 3(b), all photocatalysts exhibited a typical IR pattern of  $\text{g-C}_3\text{N}_4$ , which indicated that PCN has been loaded onto  $\text{TiO}_2$  / $\text{Zn}(\text{OAc})_2$ -ACF composites.

As shown in Fig. 4 (a), the surface of ACF modified by zinc acetate is slightly rough and owns micropores and mesopores, which provide attachment sites for photocatalytic materials and improve the adsorption performance. The pure  $\text{g-C}_3\text{N}_4$  monomer was a nano-scale tubular structure (Fig. 4(b)). From the SEM and TEM images of the PCN monomer in Fig. 4(c, d), it can be seen that PCN don't change this structure. The diameter of PCN is 98–243 nm, and the smaller diameter of PCN is conducive to the transmission of electrons and holes. At the same time, it increases the overall specific surface area and increases the active sites of contact with pollutants and photocatalytic reactions. The white spots on the surface of the PCN monomer proves that the doping of phosphorus is successful in the process of high-temperature sintering, which enhanced the photocatalytic activity of tubular  $\text{g-C}_3\text{N}_4$ . It can be seen from Fig. 4(c, e) that PCN has a massive structure and large particle size, while the PCN/ $\text{TiO}_2$  composite increases the specific surface area. Figure 4(f) and (g) are the TEM images of PCN/ $\text{TiO}_2$  composites. It can be observed that the composites are composed of black granular  $\text{TiO}_2$  and gray lamellar PCN. It is proved that  $\text{TiO}_2$  particles are uniformly distributed in the PCN tubular nanosheets, and the corresponding heterojunction (001) lattice and  $\text{TiO}_2$  anatase (101) lattice are obtained by calculating the lattice spacing. However, since PCN is a semiconductor, the PCN lattice is not measured by TEM. The SEM images of

PCN/TiO<sub>2</sub>/Zn(OAc)<sub>2</sub>-ACF composites are shown in Fig. 4(h, l). It can be observed that PCN/TiO<sub>2</sub> is successfully loaded on the surface of Zn(OAc)<sub>2</sub>-ACF.

The N<sub>2</sub> absorption desorption measurements are carried out, and the results are plotted in Fig. 5. All samples show type IV isotherms, indicating the presence of mesopores. The specific surface area, pore diameter and pore volume are shown in Table 1. The specific surface area of Zn(OAc)<sub>2</sub>-ACF is large, which can reach 1220.77 m<sup>2</sup>/g, which is because the void on the surface of ACF is not filled by catalyst particles as yet in the SEM image. And the pore diameter and specific surface area of PCN/TiO<sub>2</sub>/Zn(OAc)<sub>2</sub>-ACF are reduced due to the loading of photocatalyst(Geng et al., 2019). The pore diameter and specific surface area of 6% PCN/TiO<sub>2</sub>/Zn(OAc)<sub>2</sub>-ACF composite are the largest which are 2.73nm and 911.56m<sup>2</sup>/g, respectively. The above results are consistent with the nitrogen adsorption-desorption curve, which indicating that 6% PCN/TiO<sub>2</sub>/Zn(OAc)<sub>2</sub>-ACF has the strongest adsorption performance.

Table 1  
Textual properties of the materials

Sample	Pore size (nm)	Pore volume (cm <sup>3</sup> /g)	Specific surface area (m <sup>2</sup> /g)
ACF	2.42	0.49	1,220.77
4% PCN/TiO <sub>2</sub> /Zn(OAc) <sub>2</sub> -ACF	2.48	0.38	908.12
6% PCN/TiO <sub>2</sub> /Zn(OAc) <sub>2</sub> -ACF	2.73	0.37	911.56
8% PCN/TiO <sub>2</sub> /Zn(OAc) <sub>2</sub> -ACF	2.72	0.37	863.96

In order to study the separation, migration and recombination properties of photogenerated electron-hole pairs, photoluminescence (PL) and photocurrent response are characterized. The photoluminescence (PL) spectra of the bulk g-C<sub>3</sub>N<sub>4</sub>, PCN and PCN/TiO<sub>2</sub> are shown in Fig. 6(a). The bulk g-C<sub>3</sub>N<sub>4</sub> and PCN have strong characteristic emission peaks at 465 nm, and the peak intensity of PCN is lower than that of pure g-C<sub>3</sub>N<sub>4</sub>. This shows that the doping of appropriate P in g-C<sub>3</sub>N<sub>4</sub> greatly inhibits the recombination rate of charge carriers, thus promoting the accumulation of photoinduced electrons and holes in the conduction and valence bands of g-C<sub>3</sub>N<sub>4</sub> to produce high-concentration reactive oxygen species (e.g., ·OH and ·O<sub>2</sub><sup>-</sup>). The photoluminescence intensity of PCN/TiO<sub>2</sub> is significantly weakened, indicating that the recombination of photocarriers is inhibited by the heterojunction between TiO<sub>2</sub> and g-C<sub>3</sub>N<sub>4</sub>. The photocurrent response of PCN/TiO<sub>2</sub>/Zn(OAc)<sub>2</sub>-ACF with different mass fractions is shown in Fig. 6(b). With the deposition and sculpture-reduction process, the transient photocurrents of the samples exhibit an obvious enhancement under the continuously illumination on and off. The photocurrent response of

PCN/TiO<sub>2</sub>/Zn(OAc)<sub>2</sub>-ACF is significantly enhanced compared with bulk g-C<sub>3</sub>N<sub>4</sub>. The 6% PCN/TiO<sub>2</sub>/Zn(OAc)<sub>2</sub>-ACF has the strongest photocurrent response, where the increased photocurrent can be mainly attributed to the efficient photo-generated separation and transfer, which is beneficial to the photocatalysis and corresponds to the results.

The UV-vis diffraction spectra of the composites were characterized to study their light absorption properties and determine their band gap. The results in Fig. 7(a) show that the pure g-C<sub>3</sub>N<sub>4</sub> sample has a strong absorption band in the ultraviolet-visible region, while the anatase TiO<sub>2</sub> sample has weak visible light response. The absorption edge of TiO<sub>2</sub> and g-C<sub>3</sub>N<sub>4</sub> are about 380 nm and 470nm, respectively. Kubelka-Muck equation (Brill & Li, 2016) is used to calculate the optical gap, and the equation is shown as Eq. (2):

$$F(R) = K/S = (1-R)^2 / (2R) \quad (2)$$

where K, S, R represent absorption coefficient, reflection coefficient, diffuse reflectivity (%), respectively. The energy band gap of the TiO<sub>2</sub>/g-C<sub>3</sub>N<sub>4</sub> and PCN can be calculated by the curve of the plot of  $[F(R) \times hv]^{1/2}$  vs  $hv$  ( $h$  is Planck constant (eV·s) and  $v$  is light frequency). Substitute  $n = 1$  into the formula to get the bandgap widths of TiO<sub>2</sub>, g-C<sub>3</sub>N<sub>4</sub> and PCN which is 3.18 eV, 2.75 eV and 2.61 eV (inset in Fig. 6(a)), respectively. The band gap difference between PCN and g-C<sub>3</sub>N<sub>4</sub> is caused by P doping in PCN photocatalyst. The spectra of PCN/TiO<sub>2</sub> and PCN/TiO<sub>2</sub>/Zn(OAc)<sub>2</sub>-ACF samples have a red shift compared with those of TiO<sub>2</sub> samples. This can be attributed to the synergistic reaction between PCN and TiO<sub>2</sub>, which reduces the band gap energy and changes the optical properties. On the other hand, some chemical bonds formed between the two semiconductors may result in enhanced optical properties. In order to further study the band structure of the composites, the valence band edges (VB) of TiO<sub>2</sub>, g-C<sub>3</sub>N<sub>4</sub> and PCN are detected by VB-XPS, as shown in Fig. 7(b). When the VB edge of anatase TiO<sub>2</sub> appears at 2.54eV, the CB value is -0.64 eV. The VB edge of g-C<sub>3</sub>N<sub>4</sub> is located at 1.98 eV, and its CB is located at -0.77 eV. The VB edge of PCN is 1.78 eV and its CB is -0.83 eV. Since the CB of anatase TiO<sub>2</sub> is lower than that of PCN, there is sufficient Gibbs free energy to induce the electrons to inject from PCN into TiO<sub>2</sub>, which is conducive to separating the electron-hole pairs.

To elucidate the photocatalytic mechanism, ·OH and ·O<sub>2</sub> species of 6% PCN/TiO<sub>2</sub>/Zn(OAc)<sub>2</sub>-ACF are monitored by EPR technique using 5,5-dimethyl-1-pyrroline N-oxide (DMPO) as capture agent. As shown in Fig. 8(a,b), strong DMPO·OH peaks and DMPO·O<sub>2</sub> can be observed in the material after irradiation for 10 min and 30 min.

## 3.2 Photocatalytic performance

When 200 mg/m<sup>3</sup> n-hexane is used as the target pollutant, the effect of PCN mass fraction on the removal performance of the composite is investigated (Fig. 9 (a)). The n-hexane degradation efficiency of PCN/TiO<sub>2</sub>/Zn(OAc)<sub>2</sub>-ACF composite is higher than that of pure TiO<sub>2</sub>/Zn(OAc)<sub>2</sub>-ACF. And with the increase of PCN mass fraction, the degradation performance increases firstly and then decreases. When the mass

fraction of PCN is 6%, the removal rate of n-hexane reaches the best, which is because that the appropriate amount of phosphorus doping can enhance the visible light response of the material and improve the charge separation and transfer rate. In the reaction process, the n-hexane removal rate of composites can reach 100% within the first 30 min which is mainly due to the adsorption of ACF. With the gradual saturation of ACF, the n-hexane removal rate of the composite begins to decline. At the same time, the PCN/TiO<sub>2</sub> photocatalyst degrades the n-hexane gas adsorbed by ACF which can increase the adsorption sites of ACF, maintains the degradation performance of the composites. After about 180 min of reaction, the removal rate tends to be stable, which is because the n-hexane adsorbed by ACF in unit time reaches a dynamic equilibrium with the n-hexane degraded by photocatalyst. After 360 min of reaction, the n-hexane removal rates of pure TiO<sub>2</sub> and 2%, 4%, 6%, 8% PCN/TiO<sub>2</sub>/Zn(OAc)<sub>2</sub>-ACF are 65.86%, 76.50%, 78.35%, 90.15% and 84.50%, respectively.

When 200 mg/m<sup>3</sup> n-hexane is used as the target pollutant, 6% PCN/TiO<sub>2</sub>/Zn(OAc)<sub>2</sub>-ACF composites with calcination temperatures of 350°C, 450°C and 550°C are placed in the reactor. And n-hexane is continuously introduced to investigate the effect of calcination temperature on the n-hexane removal performance of composites (Fig. 9 (b)). With the increase in calcination temperature, the removal of n-hexane by the composite increases firstly and then decreases. At 360 min, the removal rates of n-hexane by 6% PCN/TiO<sub>2</sub>/Zn(OAc)<sub>2</sub>-ACF calcined at 350°C, 450°C and 550°C are 84.50%, 90.15% and 80.50%, respectively. It can be seen that the removal rate of the material is the highest when the calcination temperature is 450°C. BET analysis shows that with the increase of calcination temperature promotes the transformation of TiO<sub>2</sub> to the anatase phase and promotes the effective combination of PCN and TiO<sub>2</sub>, which improves photocatalytic activity. However, the decomposition reaction of PCN occurs at high temperatures, which leads to the decrease of its content in the composite. The grain size of TiO<sub>2</sub> will gradually increase at high temperatures and even appear sintering phenomenon. The specific surface area decreases and the catalytic activity is inhibited.

When 200 mg/m<sup>3</sup> n-hexane is used as the target pollutant, 6% PCN/TiO<sub>2</sub>/Zn(OAc)<sub>2</sub>-ACF composites which is dipped once, twice, three times are put into the reactor, respectively. The effect of impregnation times on the n-hexane removal performance of the composites is shown Fig. 9(c). With the increase in impregnation times, the removal efficiency of n-hexane by the composites increases firstly and then decreases. At 360 min, the removal rates of PCN/TiO<sub>2</sub>/Zn(OAc)<sub>2</sub>-ACF-1, PCN/TiO<sub>2</sub>/Zn(OAc)<sub>2</sub>-ACF-2 and PCN/TiO<sub>2</sub>/Zn(OAc)<sub>2</sub>-ACF-3 are 83.75%, 90.15% and 86.25%, respectively. It can be seen that PCN/TiO<sub>2</sub>/Zn(OAc)<sub>2</sub>-ACF-2 has the highest n-hexane removal rate. This is because the amount of PCN/TiO<sub>2</sub> loaded on ACF increases with the increase in impregnation times. Then the photocatalytic performance of the composite increases and the removal rate increases. However, after twice impregnation, the specific surface area and average pore volume of ACF decrease sharply due to excessive loading and agglomeration, so the adsorption performance of the composites for n-hexane decrease sharply. The n-hexane contact with PCN/TiO<sub>2</sub> also decreases and the photocatalytic

degradation rate of n-hexane by PCN/TiO<sub>2</sub> decreases. It also shows that there is a synergistic effect between the adsorption performance of ACF and the photocatalytic performance of PCN/TiO<sub>2</sub>.

The n-hexane with different initial concentrations is continuously injected, and 6% PCN/TiO<sub>2</sub>/Zn(OAc)<sub>2</sub>-ACF composites is put into the reactor. The effect of initial n-hexane concentration on the n-hexane removal performance of the composite is shown Fig. 10 (a). With the increase of initial concentration, the removal efficiency of n-hexane gradually decreases. At 360 min, the removal rates of 100 mg/m<sup>3</sup>, 200 mg/m<sup>3</sup>, 500 mg/m<sup>3</sup> and 1000 mg/m<sup>3</sup> are 93.25%, 90.15%, 81.25% and 59.48%, respectively. This is because the number of n-hexane molecules passing through the composite increases in unit time with the increase of initial concentration. However, the adsorption sites and photocatalytic sites of the composites are certain. In addition, too high concentration of n-hexane may cause blockage of the composites. Therefore, n-hexane removal performance decreases with the increase of initial concentration. As can be seen from Fig. 10(b), the degradation rates of n-hexane of PCN/TiO<sub>2</sub>/Zn(OAc)<sub>2</sub>-ACF under the air velocity of gases of 1000 h<sup>-1</sup>, 2000 h<sup>-1</sup>, 4000 h<sup>-1</sup> and 6000 h<sup>-1</sup> are 90.15%, 84.56% and 77.25%, 66.15%, respectively. This indicates that the removal rate decreases with the increase of the flow rate, and when the airflow velocity is 1000 h<sup>-1</sup>, the removal efficiency of n-hexane is the highest. This is due to the decrease in the residence time of n-hexane molecules on ACF as the flow rate increases, thereby reducing the degradation efficiency of PCN/TiO<sub>2</sub> photocatalysts.

The 6% PCN/TiO<sub>2</sub>/Zn(OAc)<sub>2</sub>-ACF composite is put into a self-made reactor and the n-hexane gas is injected into the reactor (Fig. 10(c)). The removal efficiency of n-hexane gas by the composites is compared under light and dark conditions. With the progress of the experiment, the photocatalytic removal performance of n-hexane will decrease with the passage of time regardless of whether the light is used. Under dark conditions, ACF gradually tends to be saturated and the degradation performance of composite materials for n-hexane begins to decline sharply which decreases to 0% in 210 min with the increase of reaction time. However, the removal rate of n-hexane by composite materials slowly decreases under light conditions. When the reaction time is about 180 min, the removal rate tends to be stable, about 90.15%. The adsorption performance of the composite increases the residence time of n-hexane, which improves the photocatalytic degradation performance of the composite for n-hexane. At the same time, PCN / TiO<sub>2</sub> catalyzes the degradation of n-hexane adsorbed by ACF, thereby increasing the free adsorption sites in ACF. The experiments show that the PCN/TiO<sub>2</sub>/Zn(OAc)<sub>2</sub>-ACF composite combines the adsorption advantage of ACF with the photocatalytic degradation advantage of PCN/TiO<sub>2</sub>, which improves the performance of hexane degradation.

It can be seen from Fig. 10(d) that the n-hexane degradation rates of 6% PCN/TiO<sub>2</sub>/Zn(OAc)<sub>2</sub>-ACF under 8W, 16W and 24W light intensity are 76.25%, 83.25% and 90.15%, respectively. The results show that the degradation efficiency of n-hexane increases gradually but not exponentially with the increase of light intensity. This is because the photon energy determines the activation energy of the reaction but the limited number of reaction points of catalysts.

The 6% PCN/TiO<sub>2</sub>/Zn(OAc)<sub>2</sub>-ACF composite is used for the cyclic experiment of photocatalytic removal of n-hexane to evaluate its photocatalytic stability. After each reaction, the composites are regenerated by calcination at high temperature (450°C). After five cycles, the removal rate of n-hexane decreases slightly from 90.15–87.34%, indicating that the catalyst has excellent stability (Fig. 11(a)). The XRD pattern of the composite material after the reaction don't change significantly (Fig. 11(b)), indicating that the composite material has excellent stability.

### 3.4 Adsorption capacity of n-hexane on PCN/TiO<sub>2</sub>/Zn(OAc)<sub>2</sub>-ACF composites

In order to analyze the adsorption performance of PCN/TiO<sub>2</sub>/Zn(OAc)<sub>2</sub>-ACF composite for n-hexane, the adsorption capacity and removal rate of ACF, PCN/TiO<sub>2</sub> and 6% PCN/TiO<sub>2</sub>/Zn(OAc)<sub>2</sub>-ACF composite for n-hexane gas are described in Fig. 12. The specific operation steps of the experiment are as follows: (i) the composite material is put into the adsorption coupled photocatalytic device, in which the stable dynamic gas is bubbling out by the bubble method; (ii) the adsorption experiment of composite materials is carried out in a lightless closed environment. (iii) under light conditions, the photocatalytic degradation of n-hexane is carried out to calculate the real-time removal rate. The experimental results show that the adsorption capacities of ACF, PCN/TiO<sub>2</sub> and PCN/TiO<sub>2</sub>/Zn(OAc)<sub>2</sub>-ACF composites for n-hexane gas are 235.5 mg/g, 16.88 mg/g and 215.3 mg/g, respectively. Although the specific surface area of 6% PCN/TiO<sub>2</sub>/Zn(OAc)<sub>2</sub>-ACF composites (911.56 m<sup>2</sup>/g ) is much smaller than that of ACF ( 1220.77 m<sup>2</sup>/g ), the adsorption capacity of 6% PCN/TiO<sub>2</sub>/Zn(OAc)<sub>2</sub>-ACF composites did not decrease significantly. This is mainly due to the existence of Ti-O or -OH bonds which providing a large number of active sites for n-hexane adsorption. Under UV irradiation, the removal efficiency of n-hexane by ACF decreases rapidly in the first four hours. With the extension of adsorption time, the adsorption equilibrium of PCN/TiO<sub>2</sub>/Zn(OAc)<sub>2</sub>-ACF composite is achieved. ACF provides abundant active sites and crisscross channels for adsorption. Interestingly, the PCN/TiO<sub>2</sub>/Zn(OAc)<sub>2</sub>-ACF composite exhibit strong n-hexane adsorption coupled photocatalytic synergy, rather than a simple linear combination of PCN/TiO<sub>2</sub> photocatalytic degradation and ACF adsorption.

### 3.5 Mechanism of photocatalysis

The synergistic mechanism of adsorption coupling photocatalysis of PCN/ TiO<sub>2</sub> / Zn(OAC) <sub>2</sub>-ACF composite on n-hexane is shown in Fig. 13. The removal of n-hexane is mainly due to the synergistic effect of ACF adsorption and photocatalytic degradation of photocatalyst PCN/TiO<sub>2</sub>. The specific steps are as follows:

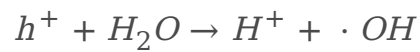
Firstly, n-hexane molecules are adsorbed on the surface of the composite, especially the active sites of ACF. It is well known that ACF is a large number of crisscross fiber rods with ravines and bulges. And the modification by zinc acetate makes its surface rougher and has more active sites. The adsorbed n-hexane on the composite promotes the close contact between n-hexane and PCN/TiO<sub>2</sub>, which accelerates the photocatalytic reaction. In addition, ACF has no photocatalytic activity as a non-semiconductor

material, but it significantly enhances the photodegradation performance of the composites by preventing electron-hole recombination, improving the photocatalytic adsorption performance and accelerating the adsorption of n-hexane on the surface of the composites. ACF in the composites has a large electron-hole pair capacity, which can accept the transferred electrons in PCN/TiO<sub>2</sub>, thereby inhibiting the recombination of electron-hole pairs (consistent with the PL spectrum (Fig. 6(a)).

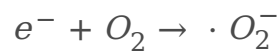
Secondly, n-hexane molecules are converted into carbon dioxide, water molecules and some intermediates under PCN/TiO<sub>2</sub> photocatalysis. Photocatalytic decomposition of n-hexane by synthetic materials is described by the following reaction Eq. (3)-(7): (Abdolahnejad et al., 2019; Thanh Truc et al., 2019; Yu et al., 2020)



3



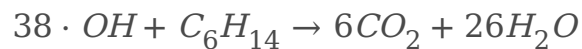
4



5



6



7

According to previous study(Wei et al., 2019), it is speculated that the intermediate products may be 2 - hexanol, 3 - hexanol, hexanone, etc.

Based on the above results, it can be concluded that the degradation mechanism of n-hexane in PCN/TiO<sub>2</sub>/Zn(OAc)<sub>2</sub>-ACF composites (Fig. 13) is an S-type heterojunction mechanism. There are three main reasons. Firstly, the VB (2.54eV) potential of TiO<sub>2</sub> is higher than the standard oxidation potential of OH<sup>·</sup>/·OH (2.4 eV vs NHE), and the VB (1.78eV) potential of PCN is lower than the standard oxidation potential of OH<sup>·</sup>/·OH (2.4eVvsNHE), so only the h<sup>+</sup> on the valence band of TiO<sub>2</sub> can produce ·OH. At the same time, because the CB (-0.83eV) potential of PCN is more negative than the standard oxidation potential of O<sub>2</sub><sup>·</sup>/·O<sub>2</sub> (-0.33 eV vs NHE), the photoinduced electrons on PCN can directly produce ·O<sub>2</sub>(Long et al., 2018). Besides, due to the high positions of CB and VB of PCN, the work function is smaller than that of TiO<sub>2</sub>. When these two semiconductors are in close contact, electrons in PCN spontaneously

diffuse to  $\text{TiO}_2$ , forming an electron depletion layer and electron accumulation layer near the interface of PCN and  $\text{TiO}_2$ , respectively.  $\text{TiO}_2$  is negatively charged and PCN is positively charged. And form the internal electric field from PCN to  $\text{TiO}_2$ . This internal electric field accelerates the transfer of photogenerated electrons from  $\text{TiO}_2$  to PCN. Secondly, the Fermi level of  $\text{TiO}_2$  surface is lower than that of PCN. When  $\text{TiO}_2$  and PCN contact, their Fermi energy should be at the same level. This causes the Fermi levels of  $\text{TiO}_2$  and PCN to move upward and downward respectively. Band bending promotes the recombination of photogenerated electrons in CB of  $\text{TiO}_2$  in the interface area and holes in VB of PCN. Thirdly, the photogenerated electrons in  $\text{TiO}_2$  CB and holes in PCN VB tend to recombine at the interface under the Coulomb attraction between holes and electrons. In conclusion, the useless electrons and holes are eliminated by recombination, while the strong photogenerated electrons in CB of PCN and holes in VB of  $\text{TiO}_2$  are retained to participate in the photocatalytic reaction (Xu, Zhang, Cheng, Fan, & Yu, 2020; Xidong Zhang et al., 2022).

Finally, the empty activated sites on ACF can continue to adsorb n-hexane molecules to realize in-situ regeneration of ACF.

## 4. Conclusions

In summary, PCN/ $\text{TiO}_2$ / $\text{Zn}(\text{OAc})_2$ -ACF was designed firstly and prepared for the dynamic degradation of n-hexane. XPS, XRD and SEM proved that P element was successfully doped into g- $\text{C}_3\text{N}_4$ , and PCN and  $\text{TiO}_2$  were successfully composited and successfully loaded onto ACF. UV-vis DRS showed that P-doped g- $\text{C}_3\text{N}_4$  resulted in band gap narrowing and spectral response expansion, and the light response of  $\text{TiO}_2$  was improved after PCN was combined with  $\text{TiO}_2$ . At the same time, PCN and  $\text{TiO}_2$  formed an S-type heterojunction, which promoted the separation and transfer of photogenerated electron-hole pairs and extended the life of charge carriers, which was confirmed by electrochemical analysis and PL spectra. Due to the synergistic effect between PCN/ $\text{TiO}_2$  and ACF, PCN/ $\text{TiO}_2$ / $\text{Zn}(\text{OAc})_2$ -ACF composite has excellent photodegradation and adsorption properties for n-hexane. Under the optimal reaction conditions (initial concentration of n-hexane  $200 \text{ mg/m}^3$ , space velocity  $1000 \text{ h}^{-1}$ , light intensity  $24 \text{ w}$ , mass fraction of doped PCN 6%, loading twice, calcination temperature  $450^\circ\text{C}$ ), the adsorption capacity of the composite was  $215.3 \text{ mg/g}$ . In addition, ACF significantly enhanced the photocatalytic activity of the composites because it could hinder the recombination of electron-hole pairs, enhance the photocatalytic adsorption capacity and accelerate the adsorption of n-hexane. Under the optimum reaction conditions, 6% PCN/ $\text{TiO}_2$ / $\text{Zn}(\text{OAc})_2$ -ACF composite showed excellent n-hexane degradation performance with a removal rate of 90.15%, which was 1.37 times higher than that of pure  $\text{TiO}_2$ / $\text{Zn}(\text{OAc})_2$ -ACF. The composites exhibit excellent stability and reusability.

## Declarations

### Acknowledgement

This research is financially supported by Shandong Natural Science Foundation Project (No. ZR2020MA104).

### Author contribution

writing✉ HaiDi Wei,EnCheng Sun;

Methodology✉Shuai Zhang,Yuxi Bi,Guoyang Ji

funding support, reviewing✉Fang Liu✉Ziyan Huang✉Chaocheng Zhao

**Data availability**Note applicable

**Ethics approval and consent to participate** Not applicable.

**Consent for publication** Not applicable.

**Competing interests** The authors declare no competing interests.

## References

1. Abdolahnejad A, Mokhtari M, Ebrahimi AA, Nikaeen M, Shahi MA, Hajizadeh Y (2019) Improved degradation of n-hexane vapours using a hybrid system, a photoreactor packed with TiO<sub>2</sub> coated-scoria granules and a multilayer biofilter. *J Environ Health Sci Eng* 17(2):1017–1027. doi:10.1007/s40201-019-00416-4
2. Bi Y, Sun E, Zhang S, Du F, Wei H, Liu F, Zhao C (2021) Synergistic effect of adsorption and photocatalysis for the degradation of toluene by TiO<sub>2</sub> loaded on ACF modified by Zn(CH<sub>3</sub>COO)<sub>2</sub>. *Environ Sci Pollut Res Int* 28(40):57398–57411. doi:10.1007/s11356-021-14539-5
3. Brill MH, Li YQ (2016) Calibrating low-scattering samples using Kubelka-Munk model. *Color Res Appl* 41(4):399–401
4. Chen P, Chen L, Ge S, Zhang W, Wu M, Xing P, He Y (2020) Microwave heating preparation of phosphorus doped g-C<sub>3</sub>N<sub>4</sub> and its enhanced performance for photocatalytic H<sub>2</sub> evolution in the help of Ag<sub>3</sub>PO<sub>4</sub> nanoparticles. *Int J Hydrog Energy* 45(28):14354–14367. doi:10.1016/j.ijhydene.2020.03.169
5. Das D, Gaur V, Verma N (2004) Removal of volatile organic compound by activated carbon fiber. *Carbon* 42(14):2949–2962. doi:10.1016/j.carbon.2004.07.008
6. Du X, Bai X, Xu L, Yang L, Jin P (2020) Visible-light activation of persulfate by TiO<sub>2</sub>/g-C<sub>3</sub>N<sub>4</sub> photocatalyst toward efficient degradation of micropollutants. *Chem Eng J* 384. doi:10.1016/j.cej.2019.123245
7. Fang H-B, Zhang X-H, Wu J, Li N, Zheng Y-Z, Tao X (2018) Fragmented phosphorus-doped graphitic carbon nitride nanoflakes with broad sub-bandgap absorption for highly efficient visible-light photocatalytic hydrogen evolution. *Appl Catal B* 225:397–405. doi:10.1016/j.apcatb.2017.11.080

8. Fu J, Xu Q, Low J, Jiang C, Yu J (2019) Ultrathin 2D/2D WO<sub>3</sub>/g-C<sub>3</sub>N<sub>4</sub> step-scheme H<sub>2</sub>-production photocatalyst. *Appl Catal B* 243:556–565. doi:10.1016/j.apcatb.2018.11.011
9. Gao H, Cao R, Xu X, Zhang S, Yongshun H, Yang H, Li J (2019) Construction of dual defect mediated Z-scheme photocatalysts for enhanced photocatalytic hydrogen evolution. *Appl Catal B* 245:399–409. doi:10.1016/j.apcatb.2019.01.004
10. Geng R, Yin J, Zhou J, Jiao T, Feng Y, Zhang L, Peng Q (2019) In Situ Construction of Ag/TiO<sub>2</sub>/g-C<sub>3</sub>N<sub>4</sub> Heterojunction Nanocomposite Based on Hierarchical Co-Assembly with Sustainable Hydrogen Evolution. *Nanomaterials (Basel)* 10(1). doi:10.3390/nano10010001
11. Guo T, Bai Z, Wu C, Zhu T (2008) Influence of relative humidity on the photocatalytic oxidation (PCO) of toluene by TiO<sub>2</sub> loaded on activated carbon fibers: PCO rate and intermediates accumulation. *Appl Catal B* 79(2):171–178. doi:10.1016/j.apcatb.2007.09.033
12. Guo Y, Wen M, Song S, Liu Q, Li G, An T (2022) Enhanced catalytic elimination of typical VOCs over ZnCoO<sub>x</sub> catalyst derived from in situ pyrolysis of ZnCo bimetallic zeolitic imidazolate frameworks. *Appl Catal B* 308. doi:10.1016/j.apcatb.2022.121212
13. Hou C, Liu H, Li Y (2021) The preparation of three-dimensional flower-like TiO<sub>2</sub>/TiOF<sub>2</sub> photocatalyst and its efficient degradation of tetracycline hydrochloride. *RSC Adv* 11(25):14957–14969. doi:10.1039/d1ra01772a
14. Hou J, Yang X, Lv X, Huang M, Wang Q, Wang J (2012) Controlled synthesis of TiO<sub>2</sub> mesoporous microspheres via chemical vapor deposition. *J Alloys Compd* 511(1):202–208
15. Huang H, Zhou C, Jiao X, Yuan H, Zhao J, He C, Steele JA (2019) Subsurface Defect Engineering in Single-Unit-Cell Bi<sub>2</sub>WO<sub>6</sub> Monolayers Boosts Solar-Driven Photocatalytic Performance. *ACS Catal* 10(2):1439–1443. doi:10.1021/acscatal.9b04789
16. Humayun M, Fu Q, Zheng Z, Li H, Luo W (2018) Improved visible-light catalytic activities of novel Au/P-doped g-C<sub>3</sub>N<sub>4</sub> photocatalyst for solar fuel production and mechanism. *Appl Catal A* 568:139–147. doi:10.1016/j.apcata.2018.10.007
17. Li QH, Dong M, Li R, Cui YQ, Xie GX, Wang XX, Long YZ (2021) Enhancement of Cr(VI) removal efficiency via adsorption/photocatalysis synergy using electrospun chitosan/g-C<sub>3</sub>N<sub>4</sub>/TiO<sub>2</sub> nanofibers. *Carbohydr Polym* 253:117200. doi:10.1016/j.carbpol.2020.117200
18. Li Z, Jiang G, Zhang Z, Wu Y, Han Y (2016) Phosphorus-doped g-C<sub>3</sub>N<sub>4</sub> nanosheets coated with square flake-like TiO<sub>2</sub>: Synthesis, characterization and photocatalytic performance in visible light. *J Mol Catal A: Chem* 425:340–348. doi:10.1016/j.molcata.2016.10.020
19. Lin C-L, Cheng Y-H, Liu Z-S, Chen J-Y (2012) Adsorption and oxidation of high concentration toluene with activated carbon fibers. *J Porous Mater* 20(4):883–889. doi:10.1007/s10934-012-9665-z
20. Liu S, Zhu H, Yao W, Chen K, Chen D (2018) One step synthesis of P-doped g-C<sub>3</sub>N<sub>4</sub> with the enhanced visible light photocatalytic activity. *Appl Surf Sci* 430:309–315. doi:10.1016/j.apsusc.2017.07.108
21. Liu ZS, Peng YH, Li WK (2014) Effects of activated carbon fibre-supported metal oxide characteristics on toluene removal. *Environ Technol* 35(9–12):1499–1507.

doi:10.1080/09593330.2013.871351

22. Long G, Ding J, Xie L, Sun R, Chen M, Zhou Y, Zhao W (2018) Fabrication of mediator-free g-C<sub>3</sub>N<sub>4</sub>/Bi<sub>2</sub>WO<sub>6</sub> Z-scheme with enhanced photocatalytic reduction dechlorination performance of 2,4-DCP. *Appl Surf Sci* 455:1010–1018. doi:10.1016/j.apsusc.2018.06.072
23. Mamaghani AH, Haghghat F, Lee C-S (2017) Photocatalytic oxidation technology for indoor environment air purification: The state-of-the-art. *Appl Catal B* 203:247–269. doi:https://doi.org/10.1016/j.apcatb.2016.10.037
24. Miyamoto J-i, Kaneko K, Kanoh H (2005) The addition of mesoporosity to activated carbon fibers by a simple reactivation process. *Carbon: An International Journal Sponsored by the American Carbon Society* 43(4):855–857
25. Raja A, Rajasekaran P, Selvakumar K, Raman G, Swaminathan M (2020) Visible active TiO<sub>2</sub>-CdS-rGO ternary nanocomposite for enhanced photodecomposition of methylene blue. *Materials Today: Proceedings*, 29, 1125–1128. doi:10.1016/j.matpr.2020.05.272
26. Sekar A, Varghese GK, Ravi Varma MK (2019) Analysis of benzene air quality standards, monitoring methods and concentrations in indoor and outdoor environment. *Heliyon* 5(11):e02918. doi:https://doi.org/10.1016/j.heliyon.2019.e02918
27. Shi J, Zheng J, Wu P, Ji X (2008) Immobilization of TiO<sub>2</sub> films on activated carbon fiber and their photocatalytic degradation properties for dye compounds with different molecular size. *Catal Commun* 9(9):1846–1850. doi:10.1016/j.catcom.2008.02.018
28. Thanh Truc NT, Pham T-D, Van Thuan D, Son LT, Tran DT, Nguyen MV, Trang HT (2019) Superior activity of Cu-NiWO<sub>4</sub>/g-C<sub>3</sub>N<sub>4</sub> Z direct system for photocatalytic decomposition of VOCs in aerosol under visible light. *J Alloys Compd* 798:12–18. doi:10.1016/j.jallcom.2019.05.236
29. Tian M-J, Liao F, Ke Q-F, Guo Y-J, Guo Y-P (2017) Synergetic effect of titanium dioxide ultralong nanofibers and activated carbon fibers on adsorption and photodegradation of toluene. *Chem Eng J* 328:962–976. doi:10.1016/j.cej.2017.07.109
30. Tran Thi VH, Lee BK (2017) Great improvement on tetracycline removal using ZnO rod-activated carbon fiber composite prepared with a facile microwave method. *J Hazard Mater* 324(Pt B):329–339. doi:10.1016/j.jhazmat.2016.10.066
31. Wang M, Tan G, Zhang D, Li B, Lv L, Wang Y, Liu Y (2019) Defect-mediated Z-scheme BiO<sub>2</sub>-x/Bi<sub>2</sub>O<sub>2.75</sub> photocatalyst for full spectrum solar-driven organic dyes degradation. *Appl Catal B* 254:98–112. doi:10.1016/j.apcatb.2019.04.044
32. Wei P, Qin D, Chen J, Li Y, Wen M, Ji Y, An T (2019) Photocatalytic ozonation mechanism of gaseous n-hexane on MO<sub>x</sub>-TiO<sub>2</sub>-foam nickel composite (M = Cu, Mn, Ag): unveiling the role of ·OH and ·O<sub>2</sub>-. *Environ Science: Nano* 6(3):959–969. doi:10.1039/c8en01291a
33. Wen C, Zhang H, Bo Q, Huang T, Lu Z, Lv J, Wang Y (2015) Facile synthesis organic-inorganic heterojunctions of HSbO<sub>3</sub>/g-C<sub>3</sub>N<sub>4</sub> as efficient visible-light-driven photocatalyst for organic degradation. *Chem Eng J* 270:405–410

34. Wu F, Ma Y, Hu YH (2020) Near Infrared Light-Driven Photoelectrocatalytic Water Splitting over P-Doped g-C<sub>3</sub>N<sub>4</sub>. *ACS Appl Energy Mater* 3(11):11223–11230. doi:10.1021/acsaem.0c02148
35. Xie T, Zhang Y, Yao W, Liu Y, Wang H, Wu Z (2019) Synthesis of Bi-deficient monolayered Bi<sub>2</sub>WO<sub>6</sub> nanosheets with enhanced photocatalytic activity under visible light irradiation. *Catal Sci Technol* 9(5):1178–1188. doi:10.1039/c8cy02344a
36. Xu Q, Zhang L, Cheng B, Fan J, Yu J (2020) S-Scheme Heterojunction Photocatalyst. *Chem* 6(7):1543–1559. doi:10.1016/j.chempr.2020.06.010
37. Yang C, Miao G, Pi Y, Xia Q, Wu J, Li Z, Xiao J (2019) Abatement of various types of VOCs by adsorption/catalytic oxidation: A review. *Chem Eng J* 370:1128–1153. doi:10.1016/j.cej.2019.03.232
38. Yi F-Y, Lin X-D, Chen S-X, Wei X-Q (2008) Adsorption of VOC on modified activated carbon fiber. *J Porous Mater* 16(5):521–526. doi:10.1007/s10934-008-9228-5
39. Yu Q, Chen J, Li Y, Wen M, Liu H, Li G, An T (2020) In-situ decoration of metallic Bi on BiOBr with exposed (110) facets and surface oxygen vacancy for enhanced solar light photocatalytic degradation of gaseous n-hexane. *Chin J Catal* 41(10):1603–1612. doi:10.1016/s1872-2067(19)63496-0
40. Zhang X, Xue Z, Li H, Yan L, Yang Y, Wang Y, Zhang W (2017) Ambient volatile organic compounds pollution in China. *J Environ Sci* 55:69–75. doi:https://doi.org/10.1016/j.jes.2016.05.036
41. Zhang X, Zeng Y, Shi W, Tao Z, Liao J, Ai C, Lin S (2022) S-scheme heterojunction of core-shell biphasic (1T-2H)-MoSe<sub>2</sub>/TiO<sub>2</sub> nanorod arrays for enhanced photoelectrocatalytic production of hydrogen peroxide. *Chem Eng J* 429. doi:10.1016/j.cej.2021.131312
42. Zhao Q, Li Y, Chai X, Xu L, Zhang L, Ning P, Tian S (2019) Interaction of inhalable volatile organic compounds and pulmonary surfactant: Potential hazards of VOCs exposure to lung. *J Hazard Mater* 369:512–520. doi:10.1016/j.jhazmat.2019.01.104
43. Ziemann PJ (2011) Effects of molecular structure on the chemistry of aerosol formation from the OH-radical-initiated oxidation of alkanes and alkenes. *Int Rev Phys Chem A* 30(2):161–195. doi:10.1080/0144235x.2010.550728

## Figures

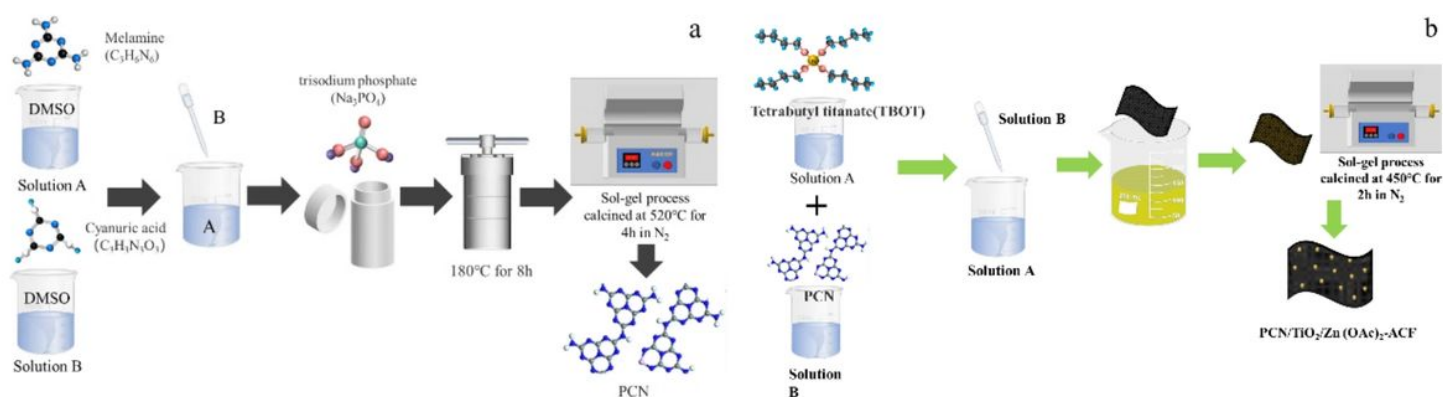


Figure 1

(a) The preparation process of PCN (b) The preparation process of PCN/TiO<sub>2</sub>/Zn(OAc)<sub>2</sub>-ACF composites

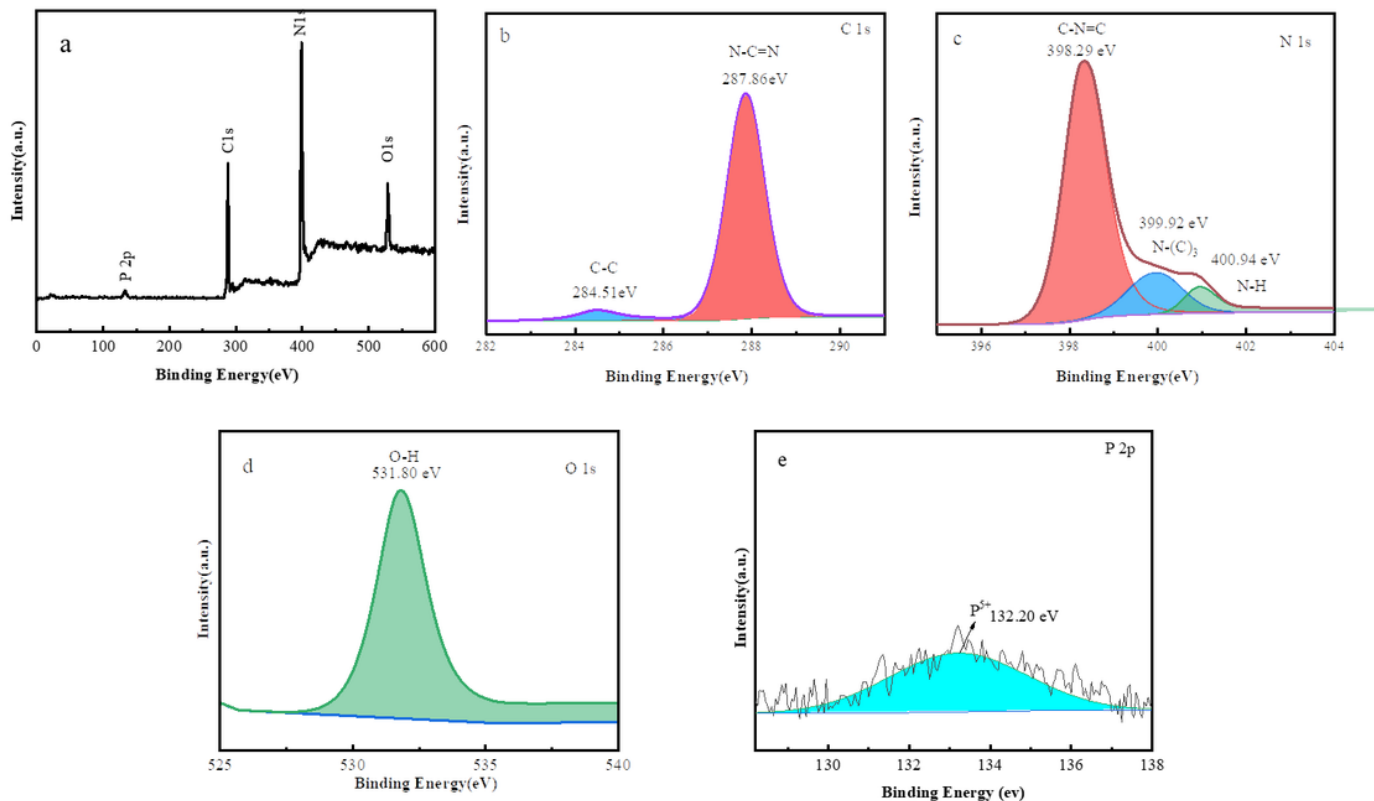
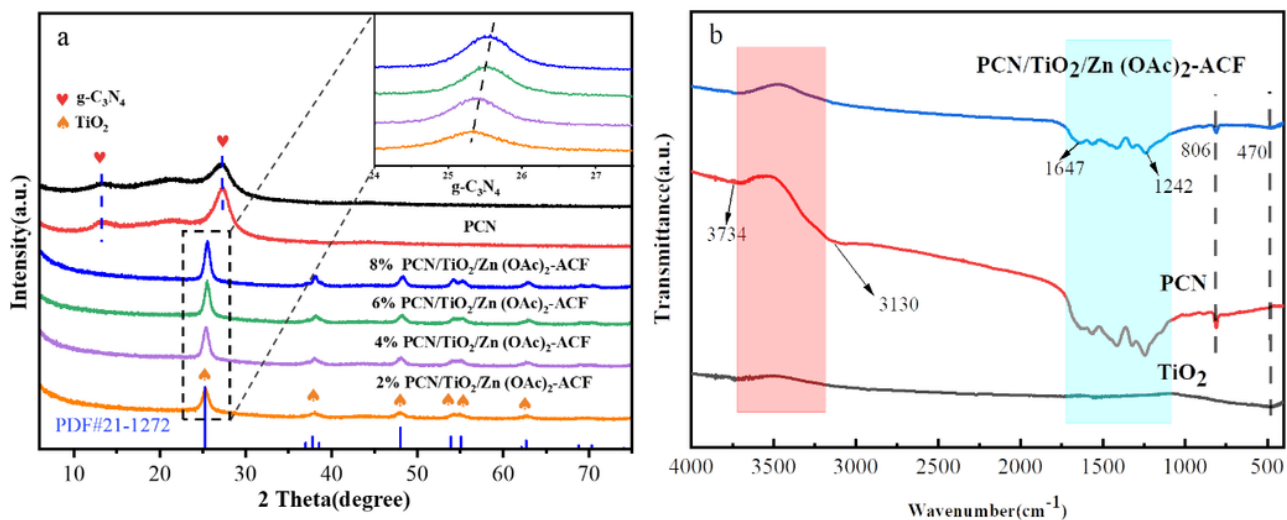


Figure 2

XPS spectra of PCN: (a) survey, (b) C 1s, (c) N 1s, (d) O 1s, (e) P 2p



**Figure 3**

3 (a) XRD patterns of pure  $g\text{-C}_3\text{N}_4$ , PCN and 2%, 4%, 6% and 8% mol PCN/TiO<sub>2</sub>/Zn(OAc)<sub>2</sub>-ACF catalysts; (b) FTIR spectra of TiO<sub>2</sub>, PCN and PCN/TiO<sub>2</sub>/Zn(OAc)<sub>2</sub>-ACF catalysts.

**Figure 4**

SEM images of Zn(OAc)<sub>2</sub>-ACF(a), pure  $g\text{-C}_3\text{N}_4$  (b), PCN (c), PCN/TiO<sub>2</sub>(e), PCN/TiO<sub>2</sub>/Zn(OAc)<sub>2</sub>-ACF (h, i) and TEM images of PCN (d), PCN/TiO<sub>2</sub> (f, g).

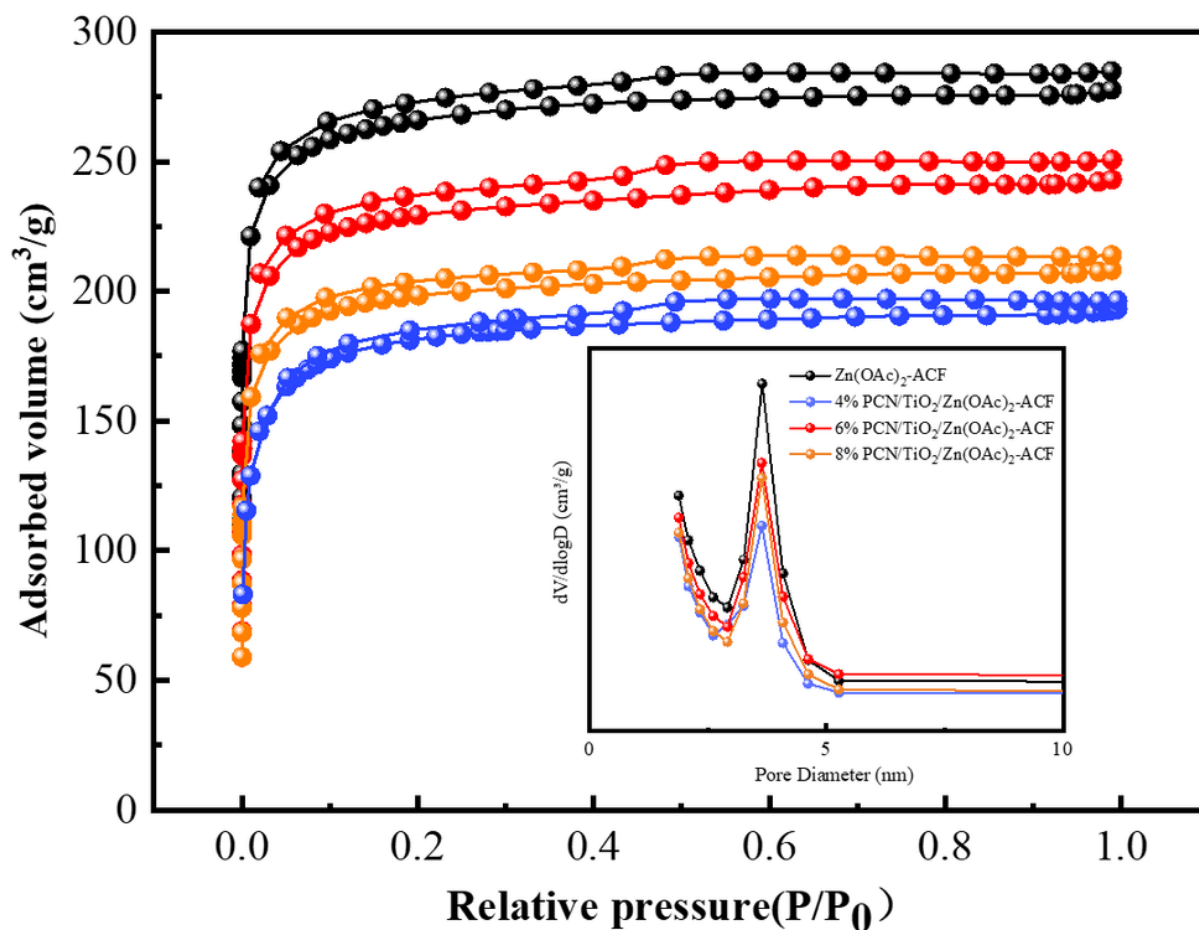


**Figure 5**

N<sub>2</sub> adsorption-desorption isotherms and the corresponding pore size distribution (inserted one) of PCN/TiO<sub>2</sub>/Zn(OAc)<sub>2</sub>-ACF samples.

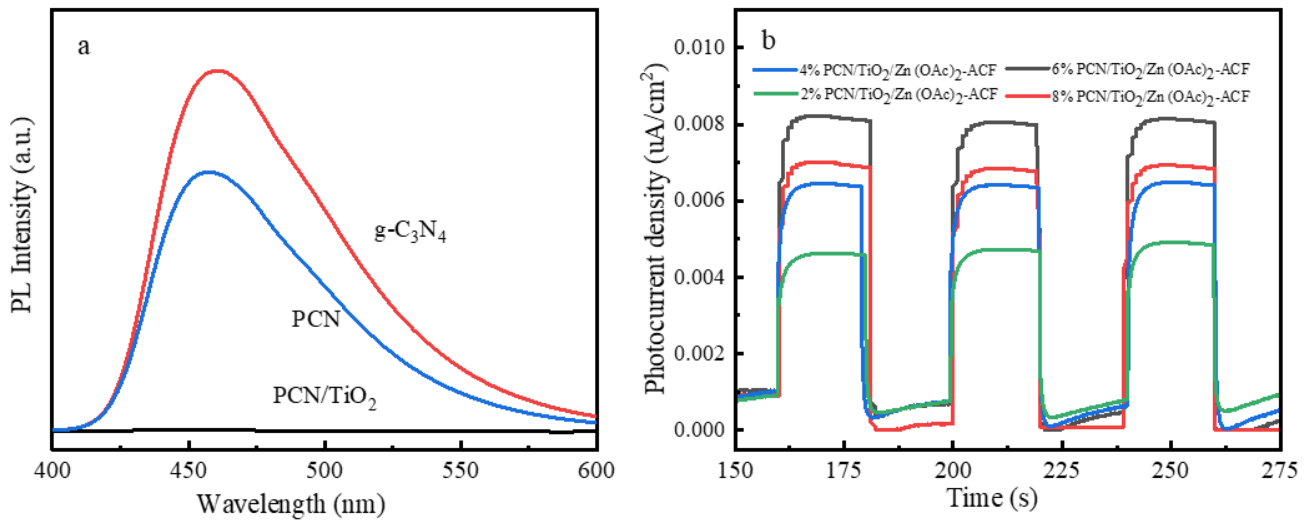


**Figure 6**

(a) PL spectra of bulk g-C<sub>3</sub>N<sub>4</sub>, PCN and PCN/TiO<sub>2</sub>; (b) Photocurrent Response Curves of 2%, 4%, 6% and 8% PCN/TiO<sub>2</sub>/Zn(OAc)<sub>2</sub>-ACF composites

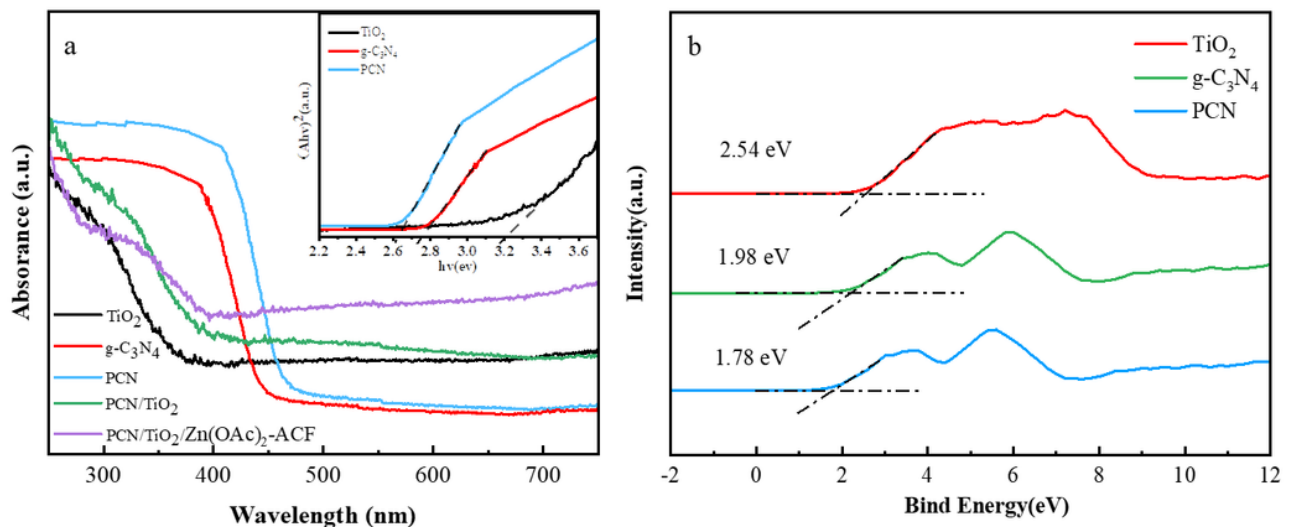


**Figure 7**

(a) UV-vis DRS spectra of TiO<sub>2</sub>, g-C<sub>3</sub>N<sub>4</sub>, PCN, PCN/TiO<sub>2</sub> and PCN/TiO<sub>2</sub>/Zn(OAc)<sub>2</sub>-ACF and the corresponding Tauc plots of (αhν)<sup>2</sup> versus hν of TiO<sub>2</sub>, g-C<sub>3</sub>N<sub>4</sub> and PCN; (b) VB-XPS of TiO<sub>2</sub>, g-C<sub>3</sub>N<sub>4</sub> and PCN

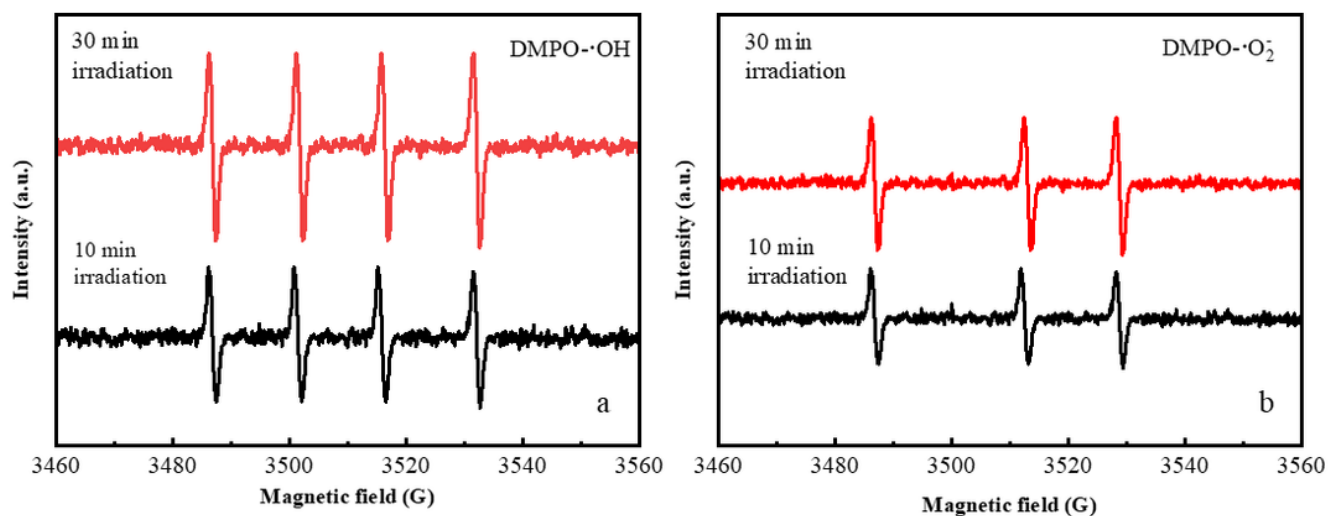


**Figure 8**

(a) EPR signals of the DMPO- $\cdot$ OH (a) and DMPO- $\cdot$ O<sub>2</sub> (b) of 6% PCN/TiO<sub>2</sub>/Zn(OAc)<sub>2</sub>-ACF, irradiated with UV-vis light for 10 min and 30min.

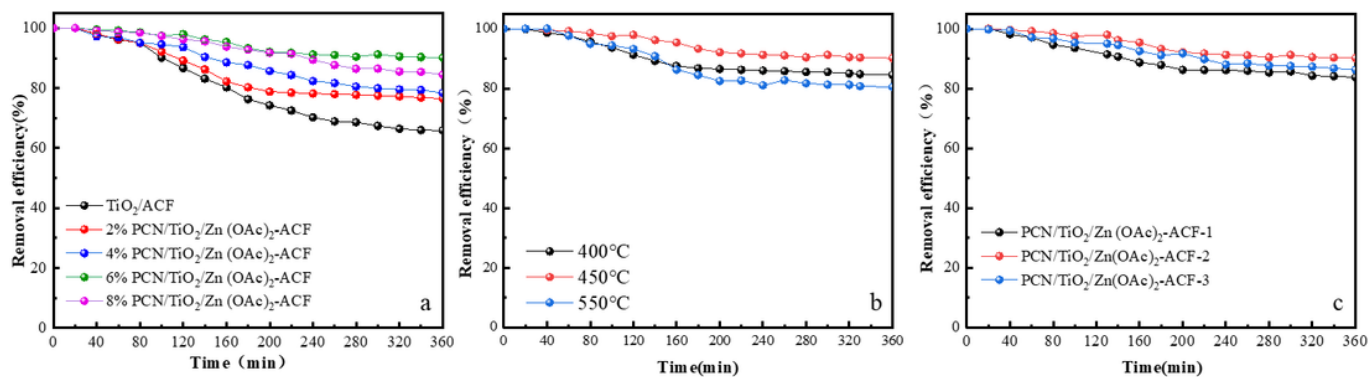


**Figure 9**

Effect on removal rate of n-hexane by (a) molar ratio of PCN, (b) calcination temperatures, (c) loading times.

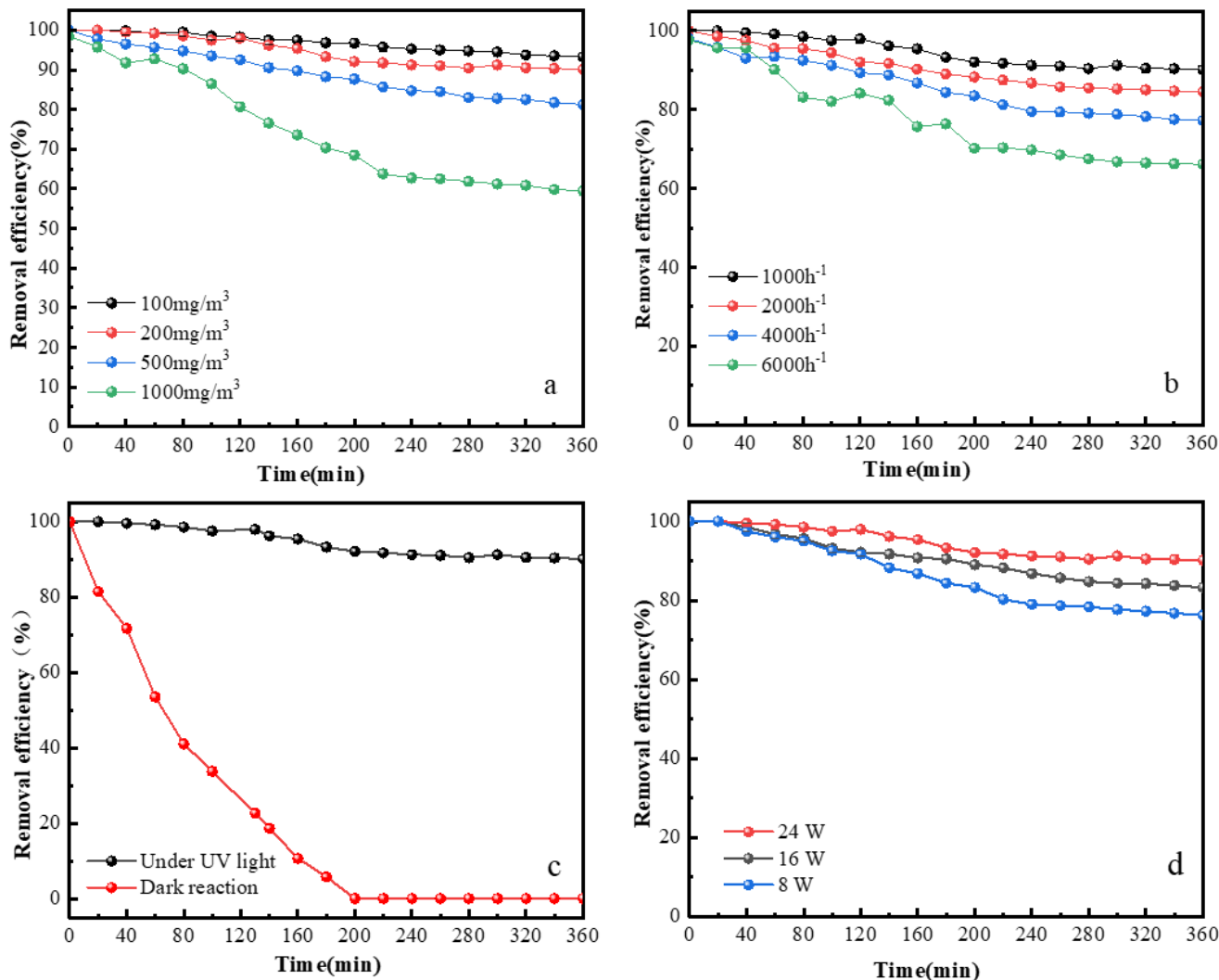


**Figure 10**

Effect on removal rate of n-hexane by (a) initial concentration of n-hexane, (b) space velocities, (d) light intensity; (c) comparison of photocatalytic and dark adsorption effects on n-hexane removal

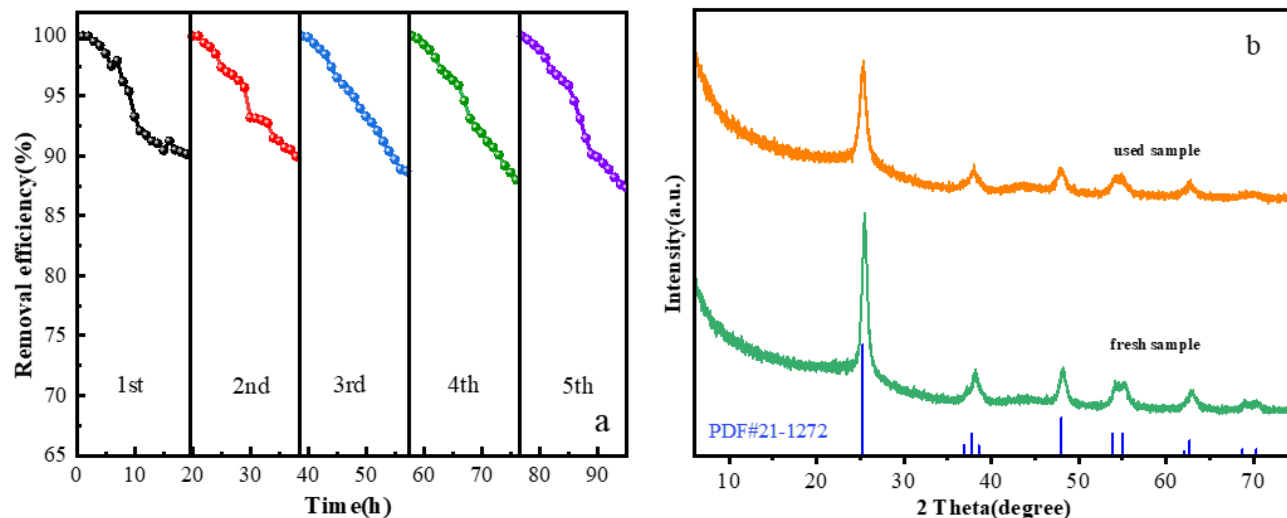


**Figure 11**

(a) Cyclic experiment of PCN/TiO<sub>2</sub>/Zn(OAc)<sub>2</sub>-ACF; (b) XRD patterns of 6% PCN/TiO<sub>2</sub>/Zn(OAc)<sub>2</sub>-ACF samples before and after five cycles

**Figure 12**

Adsorption amount and removal efficiency of n-hexane on (a) PCN/TiO<sub>2</sub>, (b) ACF, (c) PCN/TiO<sub>2</sub>/Zn(OAc)<sub>2</sub>-ACF .

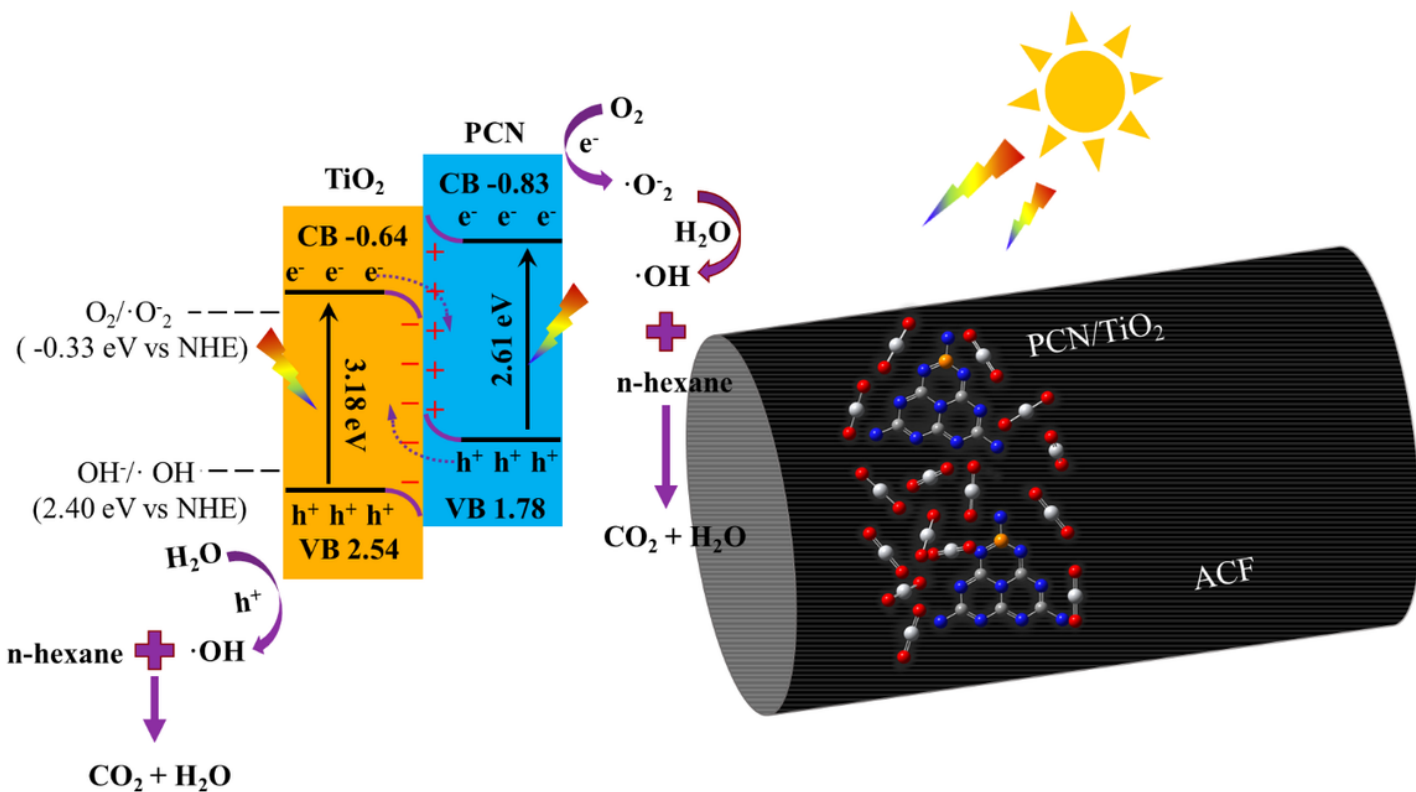


Figure 13

Schematic diagram of the mechanism of removing n-hexane from PCN/TiO<sub>2</sub>/Zn(OAc)<sub>2</sub>-ACF composites